University of Kurdistan

Dept. of Electrical Engineering

Smart/Micro Grids Research Center

Emulation of Virtual Inertia to Accommodate Higher Penetration Levels of Distributed Generation in Power Grids

Hemin Golpira, Arturo Román Messina, and Hassan Bevrani

Emulation of Virtual Inertia to Accommodate Higher Penetration Levels of Distributed Generation in Power Grids

Hêmin Golpîra, Arturo Román Messina, *Fellow, IEEE*, Hassan Bevrani, *Senior Member, IEEE*

Abstract— A novel control scheme based on a new stochastic equivalent model of the power system, which provides flexible inertia constant to enable high penetration levels of Microgrid (MG) generation is proposed. The approach combines an adaptive Energy Storage System (ESS) dispatch strategy with an MG controlled islanding scheme to provide frequency support for the host power grid. First, a Center-of-Gravity (COG) formulation of the inertia-control scheme is proposed, in which the unbalance torques between the control areas and the COG are used to reduce frequency deviations. An application example-based equivalent model of ESSs as seen from the grid side is then proposed that takes advantage of the ESS special attributes to contribute to inertial response. Simulation results on two test systems demonstrate the efficiency of the proposed control scheme to increase the host grid ability to efficiently integrate multiple MGs. Numerical tests suggest that the proposed control scheme increases system penetration level at least by 12%, which justifies the use of inertia emulation techniques to accommodate higher levels of distributed generation.

Index Terms— Adaptive control scheme, Energy storage system, Frequency nadir, High penetration, Microgrid islanding.

I. INTRODUCTION

MODERN power grids face new technical challenges arising from the increasing penetration of power-electronic-connected loads and Distributed Generation (DG) via the Microgrid (MG) concept. Paramount among these, are inertia requirement challenges as inverter-connected renewable sources are increasingly replacing synchronous generators [1]. Reduced rotational inertia in the grid may adversely affect frequency response and voltage and system control, and lead to degraded performance of traditional frequency control schemes. This, in turn, may result in large frequency deviations and, potentially, load shedding, and frequency instability [2, 3]. The increasing penetration of inverter-interfaced distributed generation motivates the need

H. Golpîra is with the Department of Electrical and Computer Engineering, University of Kurdistan, Sanandaj 66177-15175, Iran (email: hemin.golpira@uok.ac.ir)

A. R. Messina is with CINVESTAV, Guadalajara, Mexico (e-mail: arturo.roman@cinvestav.mx)

H. Bevrani is with the Department of Electrical and Computer Engineering, University of Kurdistan, Sanandaj, Iran (email: bevrani@uok.ac.ir)

to develop additional ancillary energy balancing services to control frequency changes.

Advanced control of grid-connected MGs, however, has the potential to offset the intermittent nature of distributed energy resources and provide frequency control support to the host utility during emergency conditions [4]. Successful grid integration of MGs to a utility grid requires monitoring of critical bus frequency variations and the design of adaptive frequency-based MG control schemes and improved utility-scale Energy Storage Systems (ESSs) dispatching strategies to ensure that adequate frequency control is maintained.

While numerous research works have investigated the impact of MGs and inertia-less generation on the frequency stability of bulk power systems [1, 2, 5, 6], the study of the impact of ancillary control services by DGs/MGs to accommodate higher levels of inverter-based resources has received limited attention [1]. In recent years, a number of efforts have been made to assess the effect of utility-scale ESSs in the context of determining the maximum permissible penetration level of variable generations [7-14]. These studies demonstrate the effectiveness of ESSs to provide primary frequency regulation subject to several reliability standards. Emphasis has been placed on developing suitable approaches for determining the optimum size of ESSs rather than developing ancillary control strategies to enhance dynamic behavior using the ESSs [1, 15]. In [16], an inertial emulation control strategy for frequency control of voltage source converter systems was introduced. The emulated inertia is provided by means of large capacitors. A future power-electronic based power system which mainly relies on virtual inertia is introduced in [17]. These works mainly focus on the design of control loops and power electronic aspects to emulate virtual inertia in simple systems rather than dealing with bulk system dynamics.

The lack of an accurate dynamical equivalent model of ESSs connected to distribution networks hampers the analysis of the impact of renewable power generation on transmission systems as discussed by [18] and a recent IEEE Task Force report [1]. This prevents detailed analysis of high MGs-penetrated power grid which in turn could be realized through inherent characteristics of MGs, such as controlled MG islanding.

In this paper, an equivalent model of ESSs is proposed, which can provide an appropriate framework to take

advantages of ESSs and MGs special attributes to develop new ancillary control schemes to enable high penetration of MGs. MGs and ESSs are coordinated in a frequency-based control scheme to mimic system inertia. The control scheme detects frequency events and the buses with undesired frequency behavior using a rolling window technique, frequency nadir, and Rate-of-Change-of-Frequency (RoCoF) variations following large generator and load trips. An advanced scheme that islands MGs in a multi-area system and provides virtual inertia by ESSs is then used to control power exchanges between areas to mitigate undesirable frequency deviations. The main contributions of this paper are:

- A new and flexible approach to derive a reduced-order dynamic model of the system based on a robust setting is introduced. The method extends previous formulations based on the Center-of-Gravity (COG) approach, developed by the authors, to account for the modeling of uncertain renewable generation.
- A novel ancillary control strategy to effectively increase the capability of the host grid to accommodate high penetration of MGs is proposed. The proposed approach utilizes Multi-MGs (MMGs) operating in grid-connected mode and emulates virtual inertia to provide frequency control during emergency conditions.

II. INERTIA-BASED CONTROL STRATEGY

A. Formulation of the Model

In the authors' previous work, the concept of COG was introduced to study long-term power-frequency transients following large perturbations [19]. Using the COG concept, the original power system can be represented by a simplified equivalent model (see Fig. 1) obtained by solving a simple minimization problem. Two limitations are inherent to this representation to assess the impact of MMGs integration: (a) Uncertainties in the representation of MMGs cannot be properly incorporated, and (b) Different operating modes, i.e. grid-connected and islanded modes cannot be properly represented.
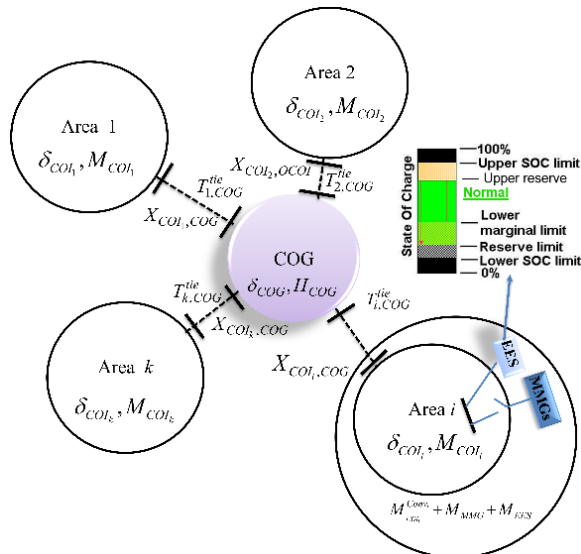

Fig. 1. Conceptual overview of the adopted control scheme showing the grid-parallel configuration of a MMGs.

Incorporating the dynamics of MMGs into the equivalent model representations requires a transformation of the simple deterministic COG formulation in [19] to a complex uncertain optimization problem. In what follows, the use of the COG framework in the case of penetrated power system with several MMGs is reviewed in the light of a robust approach to study transient frequency behavior.

To introduce the proposed formulation, assume that an interconnected power system is divided into n areas and that a Center of Inertia (COI) is associated with each area. It is assumed further that several MMGs are integrated with ESSs to provide frequency control during emergency conditions as well as to improve grid's resiliency.

Physically, the COG is a unique, fictitious location in which the resultant torque in the system vanishes, namely [19]

$$\sum_{i=1}^{n} T_{COI_i,COG}^{tie} = \sum_{i=1}^{n} \frac{P_{COI_i,COG}^{tie}}{\omega_{COG}} = 0 \tag{1}$$

Taking contribution of MMGs into account, the balance constraint (1) in the penetrated grid can be represented as

$$\sum_{i=1}^{n} T_{COI_i,COG}^{tie} = \sum_{i=1}^{n} \frac{P_{COI_i,COG}^{tie} - \Delta P_i^{MMG}}{\omega_{COG}} = 0 \tag{2}$$

where the virtual tie-line power flow, $P_{COI_i,COG}^{tie}$, has the form

$$P_{COI_i,COG}^{tie} = \frac{\left|V_{COI_i}\right|\left|V_{COG}\right|}{X_{COI_i,COG}^{tie}} \sin(\delta_{COI_i} - \delta_{COG}) \tag{3}$$

Here, ω_{COG}, ΔP_i^{MMG} are the COG angular speed and uncertain injected power of MMGs to area i, $\delta_{COI,i}$ and δ_{COG} denote respectively, the position of the COI and the COG, $V_{COI,i}$ and V_{COG} are the associated voltage magnitudes; the $X_{COI,COG}^{tie}$ is a fictitious reactance that needs to be determined. For this purpose, a four-step procedure based on a data-driven goal programming approach is proposed as follows:

Step 0: Insert (3) into (2). This results in

$$\sum_{i=1}^{n} \frac{1}{\omega_{COG}} \left(\frac{\left|V_{COI_i}\right|\left|V_{COG}\right|}{X_{COI_i,COG}^{tie}} \sin(\delta_{COI_i} - \delta_{COG}) - \Delta P_i^{MMG} \right) = 0 \tag{4}$$

Step 1: Reformulate (4) as a minimization problem

$$\min \sum_{i=1}^{n} \frac{1}{\omega_{COG}} \left(\frac{\left|V_{COI_i}\right|\left|V_{COG}\right|}{X_{COI_i,COG}^{tie}} \sin(\delta_{COI_i} - \delta_{COG}) - \Delta P_i^{MMG} \right)$$

$$s.t. \quad 0 < X_{COI_i,COG}^{tie} \leq 1 \tag{5}$$

Step 2: Recast (5) in the linear form

$$\min_{X^{tie}_{COI_i,COG}} \sum \xi^- - \xi^+$$

$$s.t. \sum_{i=1}^{n} \frac{1}{\omega_{COG}} \frac{|V_{COI_i}||V_{COG}|}{X^{tie}_{COI_i,COG}} \sin(\delta_{COI_i} - \delta_{COG}) + \xi^- - \xi^+ = \sum_{i=1}^{n} \Delta P_i^{MMG}$$

$$\xi^-, \xi^+ \geq 0$$

$$0 < X^{tie}_{COI_i,COG} \leq 1$$

$$(6)$$

where ξ^- and ξ^+ define deviations from the target value, ξ, in the positive and negative directions. Goal-programming assigns a goal value to each of the objective measures, i.e. zero to (5). Undesired deviations from the target value ξ are then minimized using (6). From linear programming theory, at least one of the ξ^- and ξ^+ must be zero [20].

Step 3: Generate scenarios for ξ and ΔP_i^{MMG}

Step 4: Re-define (6), taking the expected value of ξ into account, as

$$\min_{X^{tie}_{COI_i,COG}} \sum_{s=1}^{S} p_s \sum \xi_s^- - \xi_s^+ \qquad (7)$$

$$s.t.$$

$$\sum_{i=1}^{n} \frac{1}{\omega_{COG}} \frac{|V_{COI_i}||V_{COG}|}{X^{tie}_{COI_i,COG}} \sin(\delta_{COI_i} - \delta_{COG}) + \xi_s^- - \xi_s^+ = \sum_{i=1}^{n} \Delta P_{i,s}^{MMG}$$

$$\xi_s^-, \xi_s^+ \geq 0$$

$$0 < X^{tie}_{COI_i,COG} \leq 1$$

$$(8)$$

where p_s denotes the probability of each scenario and s denotes the scenario.

B. Rationale

Consider an equilibrium mechanical system in Fig. 2 with equilibrium point δ_0. The equilibrium condition requires that the resultant torque in the COG vanishes, namely [21],

$$F_1 \cos\delta L_1 - F_2 \cos\delta L_2 = 0; \quad F_k = m_k g h_k, \quad k = 1,2 \qquad (9\text{-}a)$$

where F, L, and δ denote the applied force, lever arm length and angle between beam and horizon, respectively. Eq. (9-a) reveals that any change in L should be compensated by F and vice versa to keep equilibrium point δ_0.
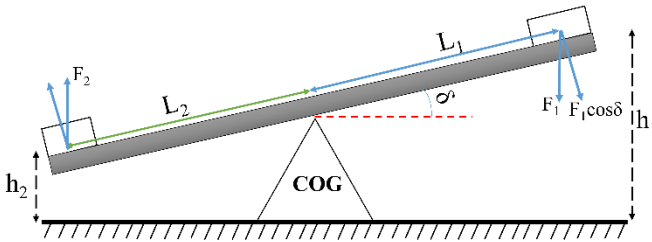

Fig. 2. Mechanical system explaining the adopted control scheme.

The same reasoning that is used in (9-a) and Fig. 2 may be applied to the equivalent model of Fig. 1. In analogy to a

mechanical system, the inertia M, can be interpreted as the mass, the fictitious reactance X is the length of the lever arm, and the inertia-weighted disturbance $\Delta P_i / M_i$ is a force. Area i in Fig.1 schematically describes the variation of L and F, through manipulation of M, in the equivalent system. Accordingly, (9-a) can be recast as

$$\frac{\Delta P_1}{M_1} X_1 + \frac{\Delta P_2}{M_2} X_2 + \frac{\Delta P_3}{M_3} X_3 + ... + \frac{\Delta P_n}{M_n} X_n = 0 \qquad (9\text{-}b)$$

The size of the inertia-weighted perturbation will cause a frequency variation, given by the swing equation [22]

$$2M \frac{df(t)}{dt} = T_m(t) - T_e(t) \qquad (10\text{-}a)$$

where, $T_m(t), T_e(t)$ are the time-varying mechanical input torque and electrical output torque, respectively. Incorporating the tie-line flows, (ΣP_{tie}), as well as the load dynamics (D), into (10-a) results in [3]

$$\dot{f} = \frac{1}{2\pi M} [\Delta P - 2\pi D \Delta f - \sum P_{tie}] \qquad (10\text{-}b)$$

According to (8), the fictitious reactance X_{COI} depends on the operating point which in turn affects frequency dynamics of interest, as will be discussed in *sub-section C*. The adopted approach relies on the following simple yet effective premise: "Any variation in the equivalent reactance, X_i in (4), following a disturbance, will be compensated by a corresponding change in $\Delta P_i / M_i$ so that the equilibrium condition is satisfied".

Referring to Fig. 1 and taking the contribution of MMGs into account, the swing equation (10) relative to the COG can be expressed in the form

$$\dot{f}_{COI_i} = \frac{1}{2\pi M_{COI_i}} [\Delta P_i - 2\pi D_i \Delta f_{COI_i} - P^{tie}_{COI_i,COG} - \Delta P_i^{MMG}]$$

$$(11)$$

Equation (11) indicates that frequency deviations exceeding a pre-determined threshold can be limited by suitable modifying the COI inertia, M_{COIi}. This, in turn, results in a change in $P^{tie}_{COI_i,COG}$ according to (3), which further affects frequency excursions. Moreover, (11) suggests that proper transition of MMGs from grid-connected mode to islanding mode can be used to aid frequency support. For area i, the total inertia can be explicitly decomposed into three constituent components, as:

$$M_i = M^{Conv.}_{COI_i} + M^{ESS} + M^{MMGs} \qquad (12)$$

where $M^{Conv.}_{COI_i}$, M^{ESS} and M^{MMGs} represent, respectively the synchronous inertia, and the inertia provided by the ESS and MMGs. Key parameters of interest to be controlled by manipulation of (12), include the frequency nadir, the RoCoF, and the frequency deviation during a given time interval of interest, i.e. a 15-second rolling window. In the proposed control scheme, the ESS output is manipulated to reduce the RoCoF and the frequency nadir through the emulated virtual inertia. Disconnecting the MMGs from the network

(islanding) in a time horizon greater than the response time of ESS, on the other hand, increases frequency evolution to satisfy the rolling window criterion. The effects of the MMGs islanding strategy on frequency response is examined based on (10) for two different operating conditions for the MG: 1) Power import from the grid, and 2) Power export to the grid. These cases are discussed separately below:

1) Power import operating mode. In the inertial response period where $T_m < T_e$, MG islanding causes the torque T_e to decrease which in turn decreases the RoCoF and nadir. On the other hand, for the time interval beyond the nadir, where $T_m > T_e$, islanding leads to a greater acceleration torque and thus a faster frequency recovery.

2) Power export operating mode. In this case, MG islanding, interpreted as a loss of inertia according to (12), renders frequency dynamics faster. The proposed control strategy imposes islanding of the MMGs beyond the frequency arrest period.

C. Frequency Sensitivity Factors

Inertia manipulation via coordinated control action of ESS and MMGs relies on the propagation of frequency dynamics in the reduced equivalent system, represented by (2)-(8). Using this notion, it is assumed that any disturbance may be aggregated and applied to the COG. Frequency deviations of the COG in (10) following a given contingency can be approximated as

$$2M_{COG}\frac{df_{COG}(t)}{dt} = \Delta R(t) - \Delta P_L \qquad (13)$$

which incorporates the additional power delivered through frequency response, i.e. R [MW], into the formulation [23]. By integrating (13) and assuming that the frequency response is delivered by linearly increasing the active power with a fixed slope (R/T_D) during inertial response [24], one could write

$$\Delta f_{COG}(t) = \frac{\frac{1}{2}\frac{R}{T_D}t^2 - \Delta P_L t}{2M} \qquad (14)$$

where, Δf_{COG}, ΔP_L, and T_D are the COG frequency deviation, imbalance power, and the delivery time of primary frequency response, respectively. The frequency nadir deviation of the COG can be calculated by setting the derivative of (14), with respect to t, to zero, namely

$$\frac{\partial|\Delta f_{COG}(t)|}{\partial t} = 0 \rightarrow \Delta f_{nadir}^{COG} = f_{nadir}^{COG} - f_0 = \frac{\Delta P_L^2 T_D}{4MR} \qquad (15)$$

Now, inserting (10) into (15) yields

$$\Delta f_{nadir}^{COG} = \frac{4M^2(\frac{d\Delta f}{dt})^2 T_D}{4MR} = \frac{M(\frac{d\Delta f}{dt})^2 T_D}{R} = \frac{M(RoCof)^2 T_D}{R} \qquad (16)$$

All the independent parameters in (15) and (16) are system-dependent except for R/T_D. As a common assumption in the calculation of maximum penetration level, the dependent

variable, i.e. Δf_{nadir}, is set to the maximum allowable value to calculate the worst case R/T_D. Accordingly, the COG frequency dynamics may be specified by (14)-(16).

The problem of interest, however, is to calculate the local dynamics of specified buses exhibiting undesired behavior. Alternatively, local behavior in (14)-(16) can be obtained using sensitivity relations in the reduced equivalent system of the form (2)-(8). Dividing (11) by (13) gives

$$\frac{df_{COI_i}}{df_{COG}} = \frac{M_{COG}}{M_{COI_i}}\frac{[\Delta P_i - 2\pi D\Delta f_{COI_i} - P_{COI_i,COG}^{tie} - \Delta P_i^{MMG}]}{(\Delta P_{mech} - \Delta P_{elec})} \qquad (17)$$

where ΔP^{MMG} defines the difference between the total generation and the local MMG load. By knowing the COG dynamics of interest in (13) and (16), and the frequency sensitivity relation in (17), one can write

$$\Delta f_{COI_i} = \frac{M_{COG}}{M_{COI_i}}\frac{[\Delta P_i - 2\pi D\Delta f_{COI_i} - P_{COI_i,COG}^{tie} - \Delta P_i^{MMG}]}{(\Delta P_{mech} - \Delta P_{elec})}\Delta f_{COG} \qquad (18)$$

or equivalently,

$$\Delta f_{COI_i} = \frac{\frac{M_{COG}}{M_i}\frac{[\Delta P_L - \sum_j P_{COI_i,COG}^{tie} - \Delta P_i^{MMG}]}{(\Delta P_{mech} - \Delta P_{elec})}}{1 + \frac{M_{COG}}{M_i}\frac{2\pi D}{(\Delta P_{mech} - \Delta P_{elec})}\Delta f_{COG}}\Delta f_{COG} \qquad (19)$$

As is apparent from (19) the MMGs capacity, ΔP^{MMG}, affects the COI dynamics through its effect on power imbalance and the associated sensitivity factor.

Let now the swing equation (10-b) be rewritten as

$$\dot{f}_j = \frac{1}{2\pi M_j}[\Delta P_j - P_{ij}^{tie} - 2\pi D_j\Delta f_j - \eta_j\Delta P_i^{MMG}] \qquad (20)$$

for bus j, where

$$\sum_j \eta_j = 1 ; \quad j \in i ; \quad \forall i \qquad (21)$$

and η_j is defined as the ratio of the total MMGs capacity at bus j to the total MMGs capacity in the associated area i. Following the same procedure as that in (19), it can be shown that

$$\Delta f_j = \frac{\frac{M_i}{M_j}\frac{[\Delta P_L - \sum_j P_{COI_i,COG}^{tie} - \Delta P_i^{MMG}]}{(\Delta P_j - P_{ij}^{tie} - \eta_j\Delta P_i^{MMG})}}{1 + \frac{M_i}{M_j}\frac{2\pi D}{(\Delta P_j - P_{ij}^{tie} - \eta_j\Delta P_i^{MMG})}\Delta f_{COI_i}}\Delta f_{COI_i} \qquad (22)$$

where M_j and M_{COG} have the same interpretation as in (12).

For each *PV* bus, the frequency nadir, the RoCoF and the frequency evolution, calculated by (19) and (22), may be compared with those of the standard values. For buses which frequency trends away from the acceptable values, dispatching of ESS and simultaneous tripping of the MMGs may be used

to change $M_{i(j)}$ and η_j to mitigate undesired frequency variations. Fig. 3 shows a flowchart representation of the proposed control scheme.
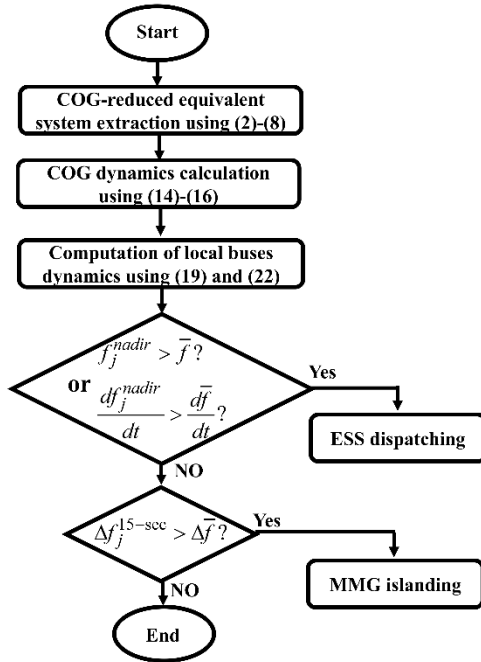

Fig. 3. Flowchart representation of the proposed control strategy; $\overline{f}$ represents an upper acceptable frequency value.

To build some intuition about the flowchart in Fig. 3, assume that the decline of frequency response of area i COI (generator j) deviates from acceptable values. Referring back to Fig. 2, and by suitably dispatching ESSs and/or MMG islanding, the position of the COI equivalent generator relative to the COG may be changed to oppose variations in frequency response. An illustration of the proposed control strategy is shown in Fig. 4 – See [25-27] for details about the internal virtual inertia loop. In a departure from previous studies, the proposed framework attempts to model the virtual inertia response, M^{ESS} rather than dealing with implementing and controlling the transfer function of the phase-locked loop (PLL), $K_f(s)$ used in voltage source converter control strategies. It should be emphasized that, the transfer function takes the State-of-Charge (SOC) and frequency indices as inputs and represents the internal inverter control strategy behavior. Using the proposed approach, the virtual inertia loop would be activated once the RoCof and frequency nadir exceed normal values following the detection of a fault.
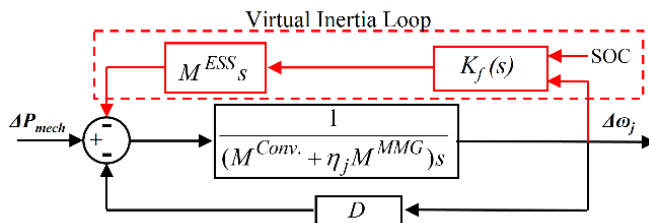

Fig. 4. Frequency response model with virtual inertia.

III. MODELING OF ENERGY STORAGE SYSTEMS (ESS)

Aside from the ESS operation mode, including grid-connected and islanded modes, the ESS status may be defined based on the SOC condition and the charge and discharge thresholds. Three levels of operation are considered (Fig. 1) [28, 29]:

- A normal operating condition in which the ESS participates in enhancing system performance.
- Upper reserve limit operation. In this case, the SOC reaches the maximum allowable value and thus the controller reduces P_{min} to zero.
- Lower SOC limit operation in which the SOC reaches the minimum allowable value. In this case, the controller forces the converter to charge the batteries.

Fig. 5 shows a block diagram representation of the SOC control architecture. Typically, the ESS includes an inverter-based source, a DC link, and an inverter firing system control, where the inverter may be treated in two different ways: islanded and grid-connected operation modes [30].
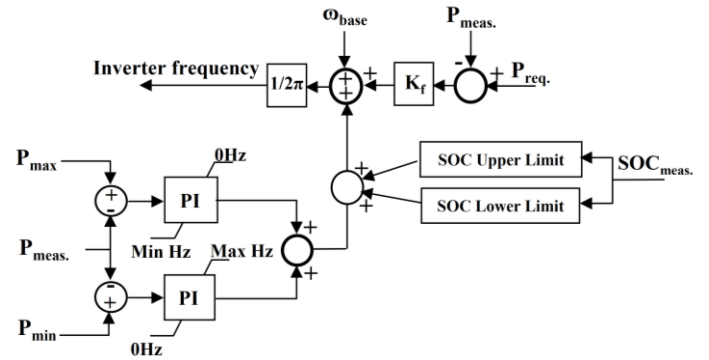

Fig. 5. Block diagram of ESSs including SOC in distribution level.

A. Visualization of ESS Behavior in Islanded Mode

Owing to the turn on/off effects of high-frequency switches, output signals have a fundamental component and higher harmonics. However, high rate of switching, in the range of 10 kHz, together with LC filters significantly mitigates harmonics [31]. Hence, the inverter, in the islanded operation mode, can be modeled as an ideal, balanced three-phase voltage source, as

$$V_{ab}^{ESS} = V_m \text{Cos}(\omega t + \theta)$$

$$V_{bc}^{ESS} = V_m \text{Cos}(\omega t + \theta + 2\pi / 3) \qquad (23)$$

$$V_{ca}^{ESS} = V_m \text{Cos}(\omega t + \theta - 2\pi / 3)$$

where V_m and ω are determined by the inverter control system. Conventional droop inverters and opposite droop inverters, as the main inverter control logics [32], are emulated through frequency and voltage droop controls.

B. ESS Equivalent Model in Grid-Connected Mode

In this section, an equivalent model for frequency response studies of a grid-connected ESS is derived. The model simply mimics a specific controlled ESS to enable assessment of the developed ancillary control scheme. As the aim is to model

and study the effects of ESS on frequency dynamics rather than dealing with the PLL controller structure and the way on which inertia is emulated, $K_f(s)$ considers to be one. Taking the slow electromechanical behavior of a Virtual Synchronous Generator (VSG) into account, such condition would be realized by appropriate setting of the PI parameters in the PLL, as discussed below.

A schematic of the ESS model is shown in Fig. 6. While the power grid in the figure refers to $M^{conv.} + \eta_j M^{MMG}$ in Fig. 4, the control algorithm block visualizes $K_f(s)$. When combined with an appropriate measurement and control strategy, this approach can be used to provide virtual inertia response and frequency support to the system, i.e. indirectly changing $M_{i(j)}$ in (19) and (22) as explained below.
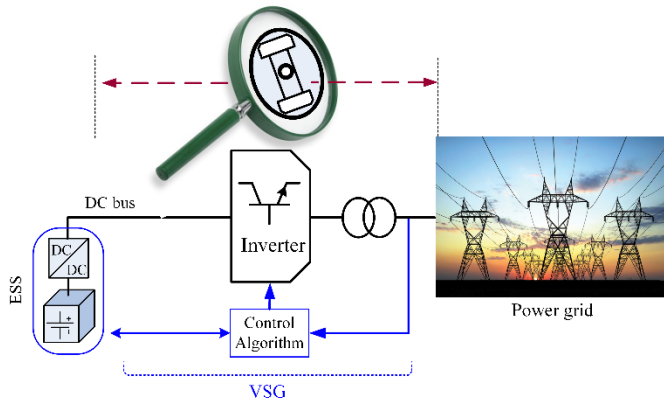

Fig. 6. Schematic of the proposed ESS dynamic equivalent model

Neglecting high frequency noise due to the switching of inverter's power transistors, the VSG appears to the network as a conventional generator and the quantity of interest is the injected power by the inverter to the grid. In this analysis, only the slow electromechanical response of the VSG is considered. Consequently, assessment of the impact of the ESS on the host grid frequency response requires mapping their associated dynamic behavior on the swing equation representation of synchronous generators. Formally, this amounts to representing the ESS dynamics by the swing equation (10) in the time domain, or equivalently, as a first-order transfer function of the form

$$\frac{f}{P_m} \propto \frac{1}{M^{ESS}s + D} \tag{24}$$

in the frequency domain. A problem that arises is that of calculating the inertia constant of the equivalent ESS and the mechanical input torque in (10) and (24). Modal analysis of the injected power from the grid to the ESS during the charging process gives

$$\frac{\omega_{MGs}}{\Delta P_{ESS}} \cong c_0 + \sum_k \frac{1}{M_k^{ESS}s + D_k} \tag{25}$$

where, ω_{MGs} and ΔP_{ESS} are the frequency at the point of common coupling and the injected power of the ESS, respectively.

Equation (25) reveals that the ESS dynamic behavior, as

seen from the utility grid, can be explained by two distinct effects: the DC term c_0 represents the requested power, i.e. P_{req} in Fig. 5, while the second term includes constituent components corresponding to (24) and can be interpreted as rotating masses with inertia constants. In our applications, (25) is obtained through modal analysis of the ESS behavior during the charging period. After the transients have settled, yet during the charging period, (25) only includes the DC term. This brings the response of RL/RC circuit to an impulse function into mind. Therefore, the same reasoning that is used to assess the response of an RL/RC circuit to an impulse function can be adopted to approximate the effects of the ESS charging/discharging dynamics. By introducing the impulse inertia into the problem formulation, one can rewrite (10) as:

$$\sum_k M_k^{ESS} \delta(\tau) \frac{df(t)}{dt} = T_m(t) - T_e(t) \tag{26}$$

where, τ is the ESS triggering time. As an impulse is not a function that can be implemented in the modeling procedure, its effect may be approximated by an exponential function of the form

$$M_k^{ESS} \delta(\tau) = M_k^{ESS} e^{-x(t-\tau)} \tag{27}$$

where, x represents an arbitrary large value that approximates the impulse characteristics of the function. Assume, to this end, that g_1 defines the frequency dynamics of the system characterized by M_k^{ESS}; accordingly, the system dynamics may be approximated as

$$h = g_1 * e^{-x(t-\tau)} \tag{28}$$

where h is the convolution of g_1 and $e^{-x(t-\tau)}$.

Except for the ESS inertia calculation, some considerations should be made regarding the mechanical input torque in (26). As an ESS has no prime mover, $T_m(t)$ in (26) is defined to have a constant value. Accordingly, inserting (27) into (26), one could write:

$$\sum_k M_k^{ESS} e^{-x(t-\tau)} \frac{df(t)}{dt} = C - T_e(t) \tag{29}$$

where C is a constant which may be determined based on the DC term of (25) in per unit. The interactions of the time varying inertia and the constant mechanical torque in (29) can be interpreted as interactions between the time-unvarying inertia and the time-varying mechanical torque in (10a) for a conventional generator. Generally, (29) reveals that the ESS would be replaced by a second-order synchronous generator model with constant mechanical input torque.

IV. SIMULATION RESULTS

A. Application example: field setup

The existing ESS in the Smart/Micro Grids Research Center (SMGRC) at the University of Kurdistan (UOK) MG is employed as application example to demonstrate efficiency of the proposed control scheme. Fig. 7 shows a three-phase diagram of UOK MG. Distributed energy resources within the MG include a 1 kW wind turbine, a 2 kW PV system, a 5 kW

diesel generator, and 2×7 kW ESSs; the MG system includes also various static and dynamic loads.
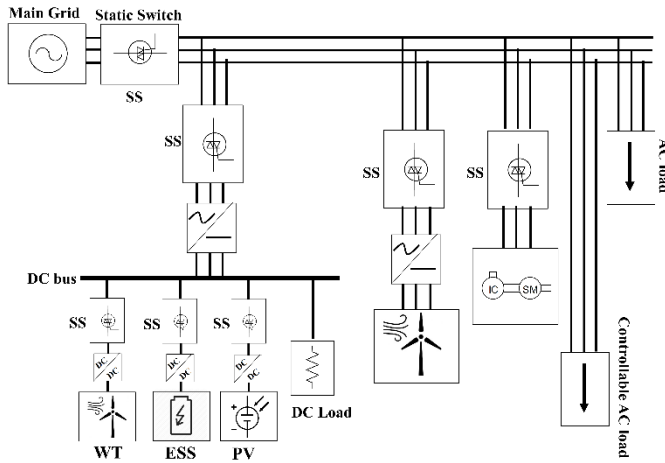

Fig. 7. Three-phase schematic representation of the UOK MG.

For the model derivation purpose, the PLL's PI parameters are set as $K_p=4$, $K_i=4$ which in turn causes $K_f(s)$ in Fig. 4 to be one. Details about the Bode diagram and the procedure of PLL parameters setting could be found in [33].

As a first test, Fig. 8 compares the SOC experimental results with those of the simulations from the ESS model in Fig. 5 for two events at about 2.5 s and 19 s, illustrating the predictive capability of the model. For event #1, when the SOC trends away from the Lower Reserve Limit (LRL), a command signal triggers the ESS to start the charging process. For event #2, where the SOC exceeds the Upper Margin Limits (UML), the discharging command returns the SOC to the normal condition. For illustration, LRL and UML are set to 50% and 50.75%, respectively (see [34] for more general modeling assumptions).
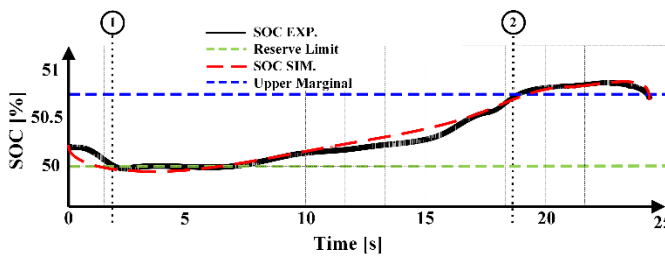

Fig. 8. Experimental and simulated response of the ESS.

To further illustrate the proposed approach, experimental results obtained from two ESSs, operating in the grid-connected mode, are used to validate the proposed equivalent model. Fig. 9 illustrates the dynamic performance of the ESSs for a sequence of events:

- Event #1. Deviation of ESS #2 from the *LRL*,
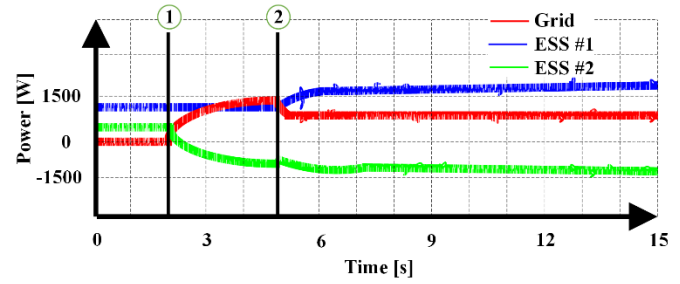- Event #2. Reduction of grid power following re-dispatching of DGs

Fig. 9. ESS and grid dynamic responses. Event #1): Charging process, and Event #2) Response to grid power reduction.

For event #1, while the ESS #2 starts the charging process in response to deviations from the minimum allowable SOC, the ESS #1 delivers power to the local loads. It can be observed that the host grid provides the required charging power of ESS #2 with some inertia constant. Event #2 refers to the reduction of the injected power of the grid in response to re-dispatching of DGs. In this case, ESS #1, which operates in normal SOC, compensates the grid power reduction and thus prevents frequency degradation.

At the same time, the SOC of ESS #2 increases towards the normal operating range. Prony (modal) analysis of the ESS #2 response, for time interval 2-5 s in Fig. 9, results in the transfer function

$$\frac{\omega^{MGs}}{\Delta P^{ESS}} \cong 1532 + \frac{0.2}{0.3+0.5s} + \frac{11.36}{0.18+0.34s} \qquad (30)$$

As suggested in (30), the ESS dynamics could be represented by two inertia constants and implemented using (28). Note that the inertia constant of the third term in (30) could be neglected for this particular test since it is significantly smaller than that of the second term. Fig. 10 compares the experimental behavior of ESSs #1 and #2 with the simulated results obtained using (30). Results reveal that the Best Fit Value (BFV) between the experimental and simulated curves is more than 95% giving a measure of modeling accuracy.
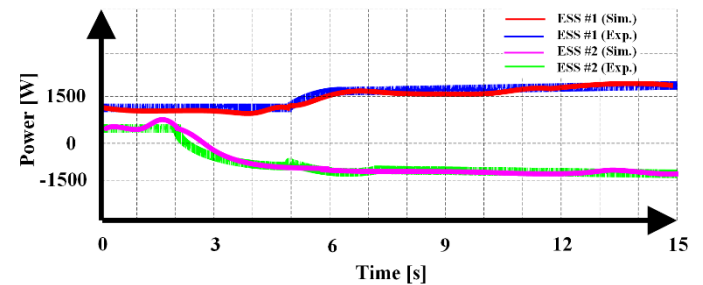

Fig. 10. Comparison of experimental (EXP) and simulated (SIM) response of ESS.

Also, of interest, Fig. 11 demonstrates the effectiveness of the equivalent model of (29) to approximate the measured long-term ESS frequency response.

Some considerations should be made regarding synchronization of MMGs and the host grid to ensure smooth voltage and current transition and safe reconnection of the two grids when the autonomous MMGs returns to the grid-connected mode of operation [35, 36]. Monitoring of the

voltage across the static switch reveals that the MMGs and the utility should be synchronized when the phase difference between voltages of the two grids is zero.
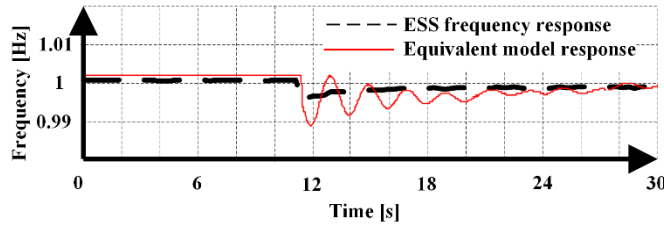

Fig. 11. Comparison of frequency response computed from experimental and equivalent model frequency response.

It should be stressed that the results presented for the UOK-MG could be elaborated to different configurations, but for the same $K_f(s)$, by considering an appropriate number of terms in (25). This is examined below by changing the configuration of the UOK-MG and grid simulator features, such as the host grid inertia. Table I shows the number of terms in (25) needed in the equivalent model of the ESS to achieve an accuracy, i.e. BFV, greater than 90%.

TABLE I
REQUIRED NUMBER OF TERMS TO BE INCLUDED IN ESS EQUIVALENT MODEL

Scenario	Grid Inertia* [s]	ESS Participating** [%]	No. of Terms
1	5	50	1
2	5	35	1
3	4	50	2
4	3	25	2
5	2	60	3

* Expressed on a 1 MW base

** ESS Participation is defined as the ratio of ESS capacity to total MG generation capacity

B. Evaluation of Control Performance

Exploratory studies to assess the impact of ESSs and MMGs islanding on system inertia and frequency dynamics control are conducted on two test systems: a) A simple two-area, four-machine test system, and b) A 16-machine, five-area 68-bus test model of the New York/New England system. Without loss of generality, a uniform distribution for the uncertain parameter ΔP^{MMGs} is considered in the studies. As a result, the derived equivalent models can be interpreted as stochastic models.

1) Two-Area System: A single-line diagram of the system is shown in Fig. 12. The total system load is 2734 MW; the disturbance considered is the trip of 1400 MW generation, i.e. $\Delta P_L=14 \; pu$, in Area 2.
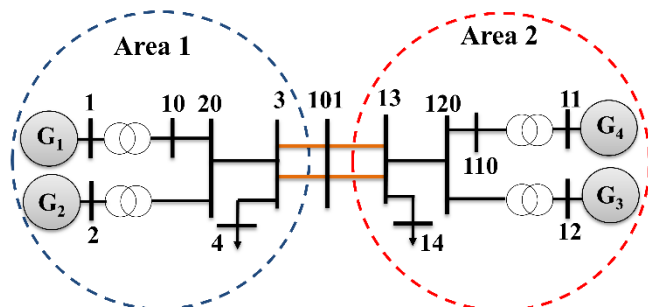

Fig. 12. Single-line diagram of the two area test system.

The reduced equivalent model of the system is constructed based on (7) and (8) to gain insight into the nature of frequency behavior. For this purpose, 10 random scenarios of equal probability, i.e. $P_s=0.1$ in (7), are generated. Minimization of (7) subject to the constraints (8) reveals that the reduced equivalent model can be characterized by

$$X^{tie}_{COI_1,COG}=0.2134 \; ; \quad X^{tie}_{COI_2,COG}=0.3172 \qquad (31)$$

Bus #1 dynamics in the conventional system, obtained by setting $\eta=0$ in (22), may be calculated by substituting (31) in (19) and (22) as

$$\Delta f_1 = \frac{1.67}{1+0.97\Delta f_{COI_1}} \Delta f_{COG} \qquad (32)$$

Similarly, for bus #12, in area two, one can obtain:

$$\Delta f_{12} = \frac{1.16}{1+0.08\Delta f_{COI_2}} \Delta f_{COG} \qquad (33)$$

Equations (32) and (33) suggest that the frequency nadir, for *PV* buses in area 2, limits the ability of the host grid to accommodate high levels of MMGs generation. A related problem of interest is that of determining the number of ESSs as well as the generation capacity of the MMGs that can be integrated into the grid to efficiently support system frequency.

From (10), the RoCoF for the base system for the perturbation of interest is

$$\frac{df_1}{dt} = \frac{14 \; pu}{M_1} \qquad (34)$$

and, for the system with high penetration of MG generation

$$\frac{df_2}{dt} = \frac{14 \; pu}{M_2} \qquad (35)$$

Dividing (35) by (34) gives

$$\frac{df_2}{df_1} = \frac{M_1}{M_2} \frac{\frac{\Delta f_1}{\Delta f_1}}{} \rightarrow \Delta f_2 = \frac{M_1}{M_2 + M^{ESS}} \Delta f_1 \qquad (36)$$

where $M_2 = M_{1+} M^{MMG}$.

Eq. (36) contains two unknown parameters, M^{ESS} and M^{MMG}. A similar expression for frequency evolution may be derived to complete the set of two independent equations. As frequency dynamics beyond the inertial response interval, is affected by MMGs islanding rather than storage support, a 15-second window starting from the nadir time is used to characterize frequency dynamics. In this case, one has that

$$f(T_n+15) - f(T_n) = \frac{\frac{1}{2}R(T_n+15) - \Delta P_L}{M_1 + M^{MMG}} - \frac{\frac{1}{2}R(T_n) - \Delta P_L}{M_1 + M^{MMG} + M^{ESS}} \qquad (37)$$

where T_n defines the time at the nadir value. Substituting the actual values ($\Delta f_1=1.1$, $M_1=2\times6.5$) and marginal quantities [37] ($\Delta f_2=0.8$, $\Delta f^{15-sec}=0.96$) in (36) and (37) show that the

ESSs should provide 0.9% of the base system inertia and that the emulated inertia is $M^{MMG}=1.4$.

Experimental results for the UOK MG show that

$$M^{MG} = 1.89 \frac{P^{Genset}}{P^{MG}} = 1.89 \frac{5}{22} = 0.43 \, [s] \tag{38}$$

where P^{Genset} and P^{MG} define the generated power of the synchronous-based DG and the overall MG generation, respectively. The inertia constant in (38) is on a 15 kW base. Accordingly, $M^{MMG}=1.4$ would be realized in the base of the system, i.e. 100 MW, by penetration of

$$P_{MMG} = \frac{1.4 \times 100}{0.43 \times 0.015} \times 0.022 = 477.52 [MW] \tag{39}$$

which allows a 17.5% penetration level of MMGs.

On the other hand, providing 0.9% of the base system inertia by ESSs results in

$$M^{ESS} = 0.009 \times M_2 = \frac{0.5 J_{VI} \omega^2 = VAh^{ESS}}{VA_{rated}} \rightarrow$$

$$0.009 \times 6.5 = \frac{VAh^{ESS}}{900} \rightarrow VAh^{ESS} = 52.65 \tag{40}$$

It then follows that the number of ESS units which could provide such energy is

$$52.65 = N \times V^{ESS} \times Ah^{ESS} = N \times 12 \times 480 \rightarrow N = 9140 \tag{41}$$

This means that 9140 ESS units, rated 12 V and 480 Ah, are required to maximize the MG penetration level. Following the same procedure as in (33), considering (41) gives

$$\Delta f_{12} = \frac{1.015}{1 + 0.01 \Delta f_{COI_2}} \Delta f_{COG} \tag{42}$$

Comparing (33) with (42) shows that the proposed control scheme can effectively reduce the frequency nadir. Fig. 13 compares the appropriateness of the adopted control strategy, assuming that, in the online control system center, the frequency event is detected after receiving 5 samples with increasing or decreasing rate [37]; in our simulations, the ESSs is triggered 0.1 sec following the inception of the fault.
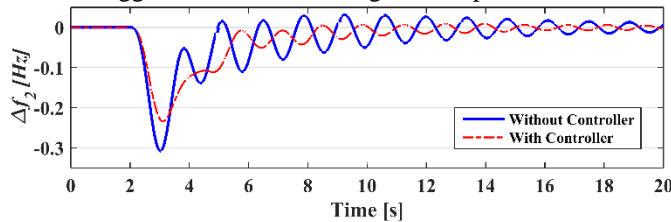

Fig. 13. ESS effect on frequency response.

2) New York/New England System: The New England test system is used to further illustrate the efficiency of the proposed control scheme. A single-line diagram of the New England system, showing major coherent areas and their interconnections, is shown in Fig. 14.
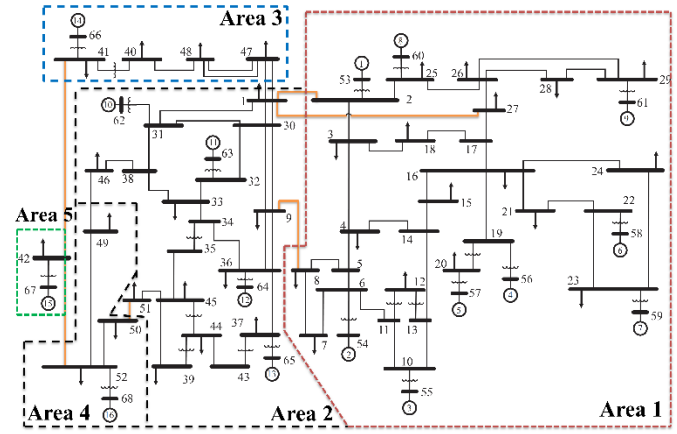

Fig. 14. Single line diagram of the 68-bus system showing coherent areas and their interconnections.

Five different contingency scenarios, including tripping of major generating units and load shedding, are considered. Results in Table II, comparing the capacity of the host grid to accommodate MG generation with and without the proposed control scheme, show the effectiveness of the proposed method.

TABLE II
COMPARISON OF MAXIMUM PENETRATION LEVEL FOR 16-MACHINE TEST SYSTEM WITH AND WITHOUT CONTROLLER

Scenario	Fault	MP* without controller [%]	MP with the proposed controller [%]	ESS/Load [%]
1	G_{12}	1.23	13.37	2.83%
2	L_{14}	1.34	15.78	3.01%
3	**G_{16}**	**0.87**	**16.11**	**2.98%**
4	L_{37}	0.56	21.06	3.54%
5	L_{42}	1.01	16.73	3.16%

MP: Maximum Penetration level

Simulation results in Table II reveal that the penetration level of MMGs into the system is limited by the frequency nadir at bus #60, in Area 1, for contingency #3. This contingency causes the COG and COI to experience frequency nadirs of 49.78 Hz and 49.89 Hz, respectively. Using (19) and (22), the frequency dynamics of bus #60 can be expressed in terms of the COG frequency behavior by the sensitivity relation

$$f_{60}^{nadir} = \frac{1.346}{1 + 0.363 f_{COI_1}} f_{COG} = \frac{1.346}{1 + 0.363(49.89/50)} 49.78 = 49.19 \tag{43}$$

Inspection of (43) shows that when the COG frequency nadir reaches 49.78 Hz, the frequency at bus #60 drops to 49.19 Hz thus limiting the penetration of distributed MG generations into the system. Installing 11 MW of ESSs at bus #60 increases the first swing frequency amplitude to 49.42 Hz and, the penetration level of Area #1 increases by 14%. Table III shows the required ESSs to increase the penetration level of MMGs obtained the procedure in (34)-(41). It should be noted that as generators G_{14}-G_{16} represent the aggregated behavior of areas 3-5 connected to the New York power system, the specification of the ESSs capacity for such equivalent areas is far from real.

TABLE III
REQUIRED ESS CAPACITY TO ENABLE HIGH PENETRATION OF MG

Scenario	Area 1 [%]*	Area 2 [%]	ESS/Load[%]**
1	5.71	3.89	2.99
2	3.89	2.03	1.82
3	5.91	4.21	3.16
4	6.33	1.70	2.39
5	3.51	4.53	2.60

*Values expressed in percentage based on each area generation capacity
**Values expressed in percentage based on total system load

Using this framework, each area in the system is characterized by two equations of the form (36) and (37). Given a system with *n* areas, solving $2 \times n$ equations allows to determine the number of ESSs and the MMGs ratings in the overall system.

Fig. 15 compares penetration levels and frequency nadirs for the system with and without the proposed controller. For completeness, the effectiveness of the proposed control scheme is compared with those strategies introduced in [38] where synchronous condensers in addition to the inertial response from wind farms are employed to enhance frequency dynamics. Simulation results demonstrate a better performance for the proposed control scheme in the present paper.
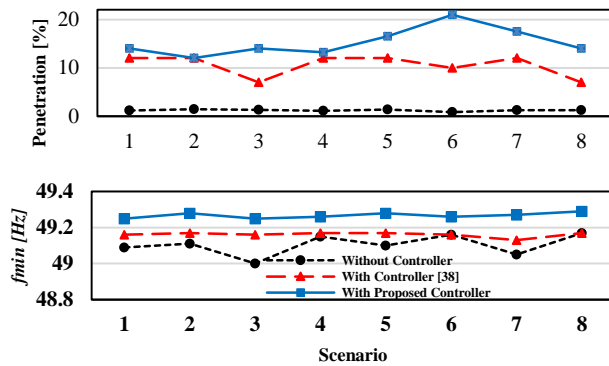

Fig. 15. Penetration level as a function of frequency nadir.

Also of interest, Fig. 16 shows time domain simulations for scenario #3. The results are associated with the reported penetration levels in Tables II and III.
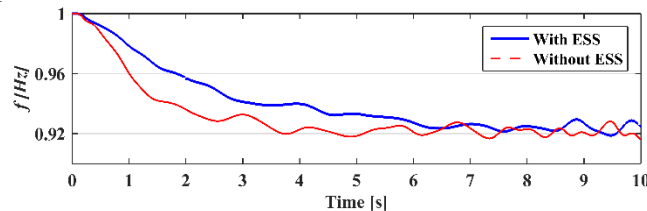

Fig. 16.ESS effect on frequency response.

Fig. 16 indicates that the *RoCoF* and frequency nadir are much less pronounced in the case with ESS that without the ESS. It should be noted that frequency nadir occurs before the 4th second of simulation, as the delivery time of primary frequency in the base system is 3.5 sec, according to [39].

In an effort to further verify the accuracy of the developed models, the effectiveness of the proposed robust model in (2)-(8) is tested for several different scenarios. Table IV compares the calculated reactance X. for different ΔP^{MMG} scenarios. In all cases, the estimated errors are below 5%. In other words,

(7) and (8) lead to a set of robust reactances, $X^{tie}_{COIi,COG}$, which would result in an accurate equivalent model for a wider range of MMGs operating conditions.

TABLE IV
COMPARISON OF FICTITIOUS REACTANCE ($X_{I, COG}$) FOR ΔP^{MMG} SCENARIOS

Scenario [P.U.]	Deterministic [19]	Robust	Error [%]
-1	0.137	0.134	2.18
-0.5	0.42	0.44	4.54
0	0.34	0.35	2.85
0.5	0.08	0.08	~0
1	0.23	0.24	4.16

V. CONCLUSIONS

In this paper, a robust framework to derive reduced-order dynamic equivalent models of an interconnected power system is introduced. The proposed model has the advantages of capturing renewable power generation uncertainties. Accordingly, a coordinated control scheme to enable high penetration levels of MMGs is proposed. The proposed control scheme relies on a robust COG-based reduced equivalent model to control imbalance torques in local areas, which in turn, provides frequency support.

The newly developed control strategy provides flexible system inertia to mitigate undesirable frequency dynamics in conformity with RoCoF, frequency nadirs and frequency evolution in a 15-second rolling window. Such flexible inertia is provided by combining an adaptive ESS dispatching with a frequency-based MMGs islanding technique. Extensive simulation results demonstrate the high efficiency of the proposed control strategy.

Results demonstrate that significant amounts of MMGs and ESSs are required to support the frequency response through such a control scheme. This amount of penetration would also increase the system equivalent droop, i.e. *R*, which may subsequently degrade the ability of the system to mitigate undesired behavior. However, analytical results reveal that the desired effect of inertia manipulation outweighs the undesired increment in *R*. Other issues such as the impact of the proposed control strategy on system damping and transient stability response are to be addressed at future stages of this research.

VI. REFERENCES

[1] N. Hatziargyriou *et al.*, "Contribution to Bulk System Control and Stability by Distributed Energy Resources connected at Distribution Network," IEEEPES-TR22, 2017.

[2] H. Golpîra, H. Seifi, A. R. Messina, and M. R. Haghifam, "Maximum Penetration Level of Micro-Grids in Large-Scale Power Systems: Frequency Stability Viewpoint," *IEEE Transactions on Power Systems,* vol. 31, no. 6, pp. 5163-5171, 2016.

[3] A. Ulbig, T. S. Borsche, and G. Andersson, "Impact of Low Rotational Inertia on Power System Stability and Operation," *arXiv preprint arXiv:1312.6435,* 2013.

[4] H. Bevrani, B. François, and T. Ise, *Microgrid Dynamics and Control.* John Wiley & Sons, 2017.

[5] P. Ferraro, E. Crisostomi, M. Raugi, and F. Milano, "Analysis of the Impact of Microgrid Penetration on Power System Dynamics," *IEEE Transactions on Power Systems,* vol. 32, no. 5, pp. 4101 - 4109, 2017.

[6] J. Varela, N. Hatziargyriou, L. J. Puglisi, M. Rossi, A. Abart, and B. Bletterie, "The IGREENGrid Project: Increasing Hosting

Capacity in Distribution Grids," *IEEE Power and Energy Magazine,* vol. 15, no. 3, pp. 30-40, 2017.

[7] V. Knap, S. K. Chaudhary, D.-I. Stroe, M. Swierczynski, B.-I. Craciun, and R. Teodorescu, "Sizing of an energy storage system for grid inertial response and primary frequency reserve," *IEEE Transactions on Power Systems,* vol. 31, no. 5, pp. 3447-3456, 2016.

[8] Y. Liu, W. Du, L. Xiao, H. Wang, and J. Cao, "A Method for Sizing Energy Storage System to Increase Wind Penetration as Limited by Grid Frequency Deviations," *IEEE Transactions on Power Systems,* vol. 31, no. 1, pp. 729-737, 2016.

[9] W.-W. Kim, J.-S. Shin, and J.-O. Kim, "Operation Strategy of Multi-Energy Storage System for Ancillary Services," *IEEE Transactions on Power Systems,* vol. 32, no. 6, pp. 4409-4417, 2017.

[10] D.-I. Stroe, V. Knap, M. Swierczynski, A.-I. Stroe, and R. Teodorescu, "Operation of a grid-connected lithium-ion battery energy storage system for primary frequency regulation: A battery lifetime perspective," *IEEE transactions on industry applications,* vol. 53, no. 1, pp. 430-438, 2017.

[11] X. Xu, H. Zhang, C. Li, Y. Liu, W. Li, and V. Terzija, "Optimization of the Event-Driven Emergency Load-Shedding Considering Transient Security and Stability Constraints," *IEEE Transactions on Power Systems,* vol. 32, no. 4, pp. 2581-2592, 2017.

[12] Y. Liu, W. Du, L. Xiao, H. Wang, S. Bu, and J. Cao, "Sizing a hybrid energy storage system for maintaining power balance of an isolated system with high penetration of wind generation," *IEEE Transactions on Power Systems,* vol. 31, no. 4, pp. 3267-3275, 2016.

[13] M. Carrión, Y. Dvorkin, and H. Pandžić, "Primary Frequency Response in Capacity Expansion With Energy Storage," *IEEE Transactions on Power Systems,* vol. 33, no. 2, pp. 1824-1835, 2018.

[14] M. Karami, H. Seifi, and M. Mohammadian, "Seamless control scheme for distributed energy resources in microgrids," *IET Generation, Transmission & Distribution,* vol. 10, no. 11, pp. 2756-2763, 2016.

[15] M. Hoffman, A. Sadovsky, M. Kintner-Meyer, and J. DeSteese, "Analysis tools for sizing and placement of energy storage in grid applications," in "Technical Report Mo. PNNL-19703," Technical Report Mo. PNNL-197032010, Available: https://goo.gl/udNWrb.

[16] J. Zhu, C. D. Booth, G. P. Adam, A. J. Roscoe, and C. G. Bright, "Inertia emulation control strategy for VSC-HVDC transmission systems," *IEEE Transactions on Power Systems,* vol. 28, no. 2, pp. 1277-1287, 2013.

[17] Q.-C. Zhong, "Power-electronics-enabled autonomous power systems: Architecture and technical routes," *IEEE Transactions on Industrial Electronics,* vol. 64, no. 7, pp. 5907-5918, 2017.

[18] F. Milano, F. Dörfler, G. Hug, D. J. Hill, and G. Verbic, "Foundations and Challenges of Low-Inertia Systems," in *20th Power System Computation Conference (PSCC), Dublin, Ireland*, 2018, pp. 11-15.

[19] H. Golpîra and A. R. Messina, "A Center-of-Gravity-Based Approach to Estimate Slow Power and Frequency Variations," *IEEE Transactions on Power Systems,* vol. 33, no. 1, pp. 1026-1035, 2018.

[20] H. M. Wagner, "Principles of operations research: with applications to managerial decisions," in *Principles of operations research: with applications to managerial decisions*: Prentice-Hall, 1969.

[21] J. L. Meriam and L. G. Kraige, *Engineering mechanics: dynamics*. John Wiley & Sons, 2012.

[22] H. Bevrani, *Robust power system frequency control*, 2nd ed. Springer, 2014.

[23] F. Teng and G. Strbac, "Full stochastic scheduling for low-carbon electricity systems," *IEEE Transactions on Automation Science and Engineering,* vol. 14, no. 2, pp. 461-470, 2017.

[24] F. Teng, V. Trovato, and G. Strbac, "Stochastic scheduling with inertia-dependent fast frequency response requirements," *IEEE Transactions on Power Systems,* vol. 31, no. 2, pp. 1557-1566, 2016.

[25] J. Fang, H. Li, Y. Tang, and F. Blaabjerg, "Distributed power system virtual inertia implemented by grid-connected power converters," *IEEE Transactions on Power Electronics,* vol. 33, no. 10, pp. 8488-8499, 2018.

[26] C. Li, J. Xu, and C. Zhao, "A coherency-based equivalence method for MMC inverters using virtual synchronous generator control," *IEEE Transactions on Power Delivery,* vol. 31, no. 3, pp. 1369-1378, 2016.

[27] S. D'Arco, J. A. Suul, and O. B. Fosso, "A Virtual Synchronous Machine implementation for distributed control of power converters in SmartGrids," *Electric Power Systems Research,* vol. 122, pp. 180-197, 2015.

[28] R. Lasseter and M. Erickson, "Integration of battery-based energy storage element in the CERTS microgrid," in "CERTS Final Report, University of Wisconsin-Madison," 2009.

[29] M. J. Erickson and R. H. Lasseter, "Integration of battery energy storage element in a CERTS microgrid," in *2010 IEEE Energy Conversion Congress and Exposition*, 2010, pp. 2570-2577: IEEE.

[30] J. Rocabert, A. Luna, F. Blaabjerg, and P. Rodriguez, "Control of power converters in AC microgrids," *IEEE transactions on power electronics,* vol. 27, no. 11, pp. 4734-4749, 2012.

[31] M. Lemmon, "Comparison of Hardware Tests with SIMULINK Models of UW Microgrid," in "Technical Report, University of Notre Dame," 2010.

[32] C.-C. Chang, D. Gorinevsky, and S. Lall, "Dynamical and voltage profile stability of inverter-connected distributed power generation," *IEEE Transactions on Smart Grid,* vol. 5, no. 4, pp. 2093-2105, 2014.

[33] Y. Sun, "The impact of voltage-source-converters' control on the power system: the stability analysis of a power electronics dominant grid," *Technical Report,* 2018.

[34] H. Bevrani, T. Ise, and Y. Miura, "Virtual synchronous generators: A survey and new perspectives," *International Journal of Electrical Power & Energy Systems,* vol. 54, pp. 244-254, 2014.

[35] R. H. Lasseter, "Control and design of microgrid components," *PSERC Publication 06-03,* 2006.

[36] C.-L. Chen, Y. Wang, J.-S. Lai, Y.-S. Lee, and D. Martin, "Design of parallel inverters for smooth mode transfer microgrid applications," *IEEE Transactions on Power Electronics,* vol. 25, no. 1, pp. 6-15, 2010.

[37] *Standard BAL-003-1—Frequency Response and Frequency Bias Setting*, 2013.

[38] A. S. Ahmadyar, S. Riaz, G. Verbič, A. Chapman, and D. J. Hill, "A framework for assessing renewable integration limits with respect to frequency performance," *IEEE Transactions on Power Systems,* vol. 33, no. 4, pp. 4444-4453, 2018.

[39] GE, "Frequency Response: Basics," GE Energy, USA2010.

Hêmin Golpîra received the B.Sc., M.Sc., and Ph.D. degrees in electrical engineering in 2007, 2009, and 2014, respectively, all with honors.

During 2014 and 2015 He was with the University of Wisconsin-Madison, Wisconsin, USA, as Associate Fellow. In 2016, he joined the University of Kurdistan, Sanandaj, Iran, as assistant professor. His current research interests include power system dynamics and stability, renewable energy integration, power system modeling & simulation and wide area monitoring and control.

Arturo Román Messina (M'85-SM'05–F'12) received the M.Sc. degree (Honors) in electrical engineering from the National Polytechnic Institute of Mexico, Mexico City, in 1987, and the Ph.D. degree from Imperial College, London, U.K., in 1991.

Since 1997, he has been a Professor at the Center for Research and Advanced Studies (CINVESTAV), Guadalajara, Mexico**.**

Hassan Bevrani (S'90-M'04-SM;08) received PhD degree in Electrical Engineering from Osaka University in 2004. Currently, he is a full professor, the Program Leader of Micro/Smart Grids Research Center (SMGRC), and Vice Chancellor for Research at the University of Kurdistan. Over the years, he has worked with Osaka University, Kumamoto University (Japan), Queensland University of Technology (Australia), Kyushu Institute of Technology, Centrale Lille (France), and Technical University of Berlin (Germany). He is the author of 6 international books, 15 book chapters, and more than 300 journal/conference papers. His current research interests include Smart grid operation and control, power system stability, Microgrid dynamics and control, and Intelligent/robust control applications in power electric industry.